Nano Research

Open Access

Research Article

Electrochemical anchoring of rhenium single atoms on NiCoMo-Se heterostructure electrocatalyst for ampere-level hydrogen evolution

Xuewen Xia[1], Xueqiang Zhang[1], Nannan Zhang[1], Xin Yuan[1], Yaofei Mu[1], Shujuan Wang[2] ✉, Ya Gao[1], Zhongya Pang[1], Xing Yu[1], Guangshi Li[1], Shen Hu[3], Li Ji[3], Xionggang Lu[1] ✉, and Xingli Zou[1] ✉

[1] *State Key Laboratory of Advanced Refractories & School of Materials Science and Engineering, Shanghai University, Shanghai 200444, China*
[2] *Shanghai Institute of Applied Physics, Chinese Academy of Sciences, Shanghai 201800, China*
[3] *School of Microelectronics, Fudan University, Shanghai 200433, China*

Cite this article: *Nano Research*, **2026**, *19*, 94908569. https://doi.org/10.26599/NR.2026.94908569

ABSTRACT: The development of high-performance and non-platinum electrocatalysts capable of operating at industrial-scale current densities is crucial for cost-effective green hydrogen production. While rhenium (Re) exhibits promising attributes, its implementation is hindered by the difficulty in synthesizing metallic Re and the suboptimal activity of its bulk forms. Herein, we demonstrate a facile electrochemical strategy to immobilize Re single atoms onto a Co, Mo-doped $NiSe_2$/NiCoMo alloy heterostructure (Re_{SA}-NiCoMo-Se) in a deep eutectic solvent. The optimized electrocatalyst delivers exceptional hydrogen evolution reaction (HER) performance in alkaline media, requiring ultralow overpotentials of only 23 and 292 mV at current densities of 10 and 1000 mA·cm^{-2}, respectively. When configured as a cathode in a flowing alkaline water electrolyzer, it enables competitive water splitting performance and robust operational stability for over 500 h. Structural characterization and theoretical calculations reveal that the atomically dispersed Re sites act as the active centers to facilitate the water dissociation and optimize hydrogen adsorption energy, simultaneously triggering a profound electron redistribution within the heterostructure support that leads to a collective enhancement of the reaction kinetics. This study showcases the feasibility of synthesizing Re single-atom materials via the electrochemical approach and highlights their potential as high-performance and stable electrocatalysts suitable for industrial applications.

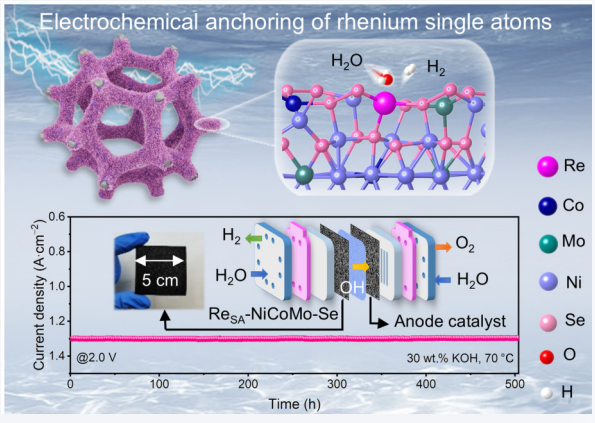

KEYWORDS: rhenium single-atoms, heterostructures, electrodeposition, deep eutectic solvents, alkaline hydrogen evolution

1 Introduction

Water electrolysis is an efficient and environmentally friendly technology for hydrogen production without emitting carbon-containing pollutants [1, 2]. The hydrogen evolution reaction (HER) in alkaline conditions shows significant potential for large-scale hydrogen production, but is hampered by slow reaction kinetics, particularly in the water dissociation step [3]. Therefore, developing efficient and durable electrocatalysts for HER is crucial to addressing this challenge [4]. While noble metals like Pt, Ir, and Ru are common HER catalysts, their high cost and scarcity hinder widespread industrial application [5]. Thus, there is an urgent need to balance catalytic performance and cost control by reducing the usage of precious metals or developing non-noble alternatives. Recently, rhenium (Re) has gained increasing attention as a promising HER catalyst due to its theoretical high activity indicated by the Trasatti volcano plot and its suitability for alkaline environments as suggested by the Pourbaix diagram [6, 7]. Besides, as of 2025, the price of Re is about 4.48% of Pt [8]. However, bulk metallic Re electrodes exhibits relatively high overpotentials for HER (> 200–300 mV at 10 mA·cm$_{geo}^{-2}$, where cm$_{geo}^{-2}$ shows the surface unit based on the geometrical surface) [9], restricting their

Received: November 18, 2025; **Revised:** January 20, 2026
Accepted: February 13, 2026

✉Address correspondence to Shujuan Wang, wangshujuan@sinap.ac.cn; Xionggang Lu, luxg@shu.edu.cn; Xingli Zou, xlzou@shu.edu.cn

practical application. The production of high-purity Re typically involves complex processes including hydrogen reduction and vacuum distillation of zone recrystallization, while direct electrochemical deposition of Re is considered as one of the most promising preparation routes [10]. Nevertheless, studies have shown that the conversion of prevalent ReO_4^- precursors to metallic Re^0 involves multiple reduction steps and tends to form rhenium oxides byproducts (predominantly ReO_2 and ReO_3) [11–13], making the electrochemical synthesis of Re particularly complex. Moreover, the low deposition overpotential of Re in aqueous solutions leads to intense competition with the HER [14, 15], making Re one of the most challenging metal systems to electrodeposit efficiently.

Given the challenges in synthesizing bulk Re electrodes and their limited catalytic efficiency, research focus has shifted toward Re-based compounds such as sulfides, selenides, and oxides [9]. In recent years, the single atom catalysis strategy has opened new avenues for the development of Re-based materials toward energy storage and conversion reaction, such as HER, oxygen evolution reaction (OER), oxygen reduction reaction (ORR), and CO_2 conversion [16–18]. Anchoring Re as single atoms on suitable supports (e.g., carbon and metal oxides/sulfides) significantly improves intrinsic activity [19–21]. As for HER, Yu et al. reported that a single-atomic Re-assisted 2H-1T phase MoS_2 delivered a small overpotential of 38 mV to achieve 10 $mA·cm^{-2}$ in alkaline media [22]. Similarly, Zhang et al. presented a Re-MoS_2-Vs electrocatalyst incorporating single-atom Re with the adjacent S vacancies, demonstrating a comparable overpotential of 99 mV at 10 $mA·cm^{-2}$ and operational stability over 120 h [23]. Peng et al. fabricated a Re-CoS catalyst that demonstrates a low overpotential of 72 mV at 10 $mA·cm^{-2}$, along with 200 h of stability [24]. These advances highlight that single-atom Re can effectively modulate the electronic structure of metal sulfides support, thereby enhancing hydrogen evolution efficiency. However, further research and design are needed to develop Re single-atom catalysts anchored on other robust supports that possess both high activity and stability for industrial applications. Transition metal selenides (TMSes) are attractive two-dimensional (2D) supports for anchoring single atoms, owing to their unique layered structures, high activity, stability, and cost-effectiveness [25]. Besides, the electrocatalytic performance of TMSes can be further enhanced through strategies like heteroatom doping and heterostructure construction [26–28]. Nevertheless, fabricating highly active and stable Re single-atom catalysts based on TMSes and elucidating the underlying enhancement mechanisms remain critical challenges.

Electrochemical techniques offer the benefits of straightforward operation and potential for industrial scale-up, and have been utilized in the synthesis of diverse single-atom catalysts (SACs) [29–31]. Furthermore, opting for ionic liquids or deep eutectic solvents (DESs) over conventional aqueous solutions as electrolyte can yield a moderate electrochemical reaction rate and a broader electrochemical window, thereby providing favorable conditions for electrosynthesis of Re single-atom materials [32, 33]. Herein, an electrochemical approach was utilized to fabricate a Co, Mo-doped nickel selenide/NiCoMo alloy heterostructure (denoted as NiCoMo-Se) to serve as a platform for immobilizing individual Re atoms. Subsequently, the metallic bulk Re was converted into single-atomic Re and then anchored on the NiCoMo-Se via a precisely controlled electrodeposition process in a choline chloride-glycol DES. The optimized electrocatalyst, named as Re_{SA}-NiCoMo-Se, showed excellent catalytic performance for the HER with small overpotentials of 23 and 292 mV at 10 and 1000 $mA·cm^{-2}$, respectively. Moreover, a comparable cell voltage of 1.91 V at 1000 $mA·cm^{-2}$ and a satisfactory long-term stability over 500 h are achieved by applying the Re_{SA}-NiCoMo-Se as cathode in flowing alkaline water electrolyzer (AWE) device with 30 wt.% KOH solution at 70 °C. Density functional theory (DFT) results demonstrated that the incorporation of the Re single atoms significantly adjusts the electronic structure of NiCoMo-Se, optimizes the hydrogen adsorption/desorption free energy, and further enhances the conductivity and electrocatalytic reaction kinetics. This work provides a new strategy for developing high-performance Re SACs for industrial applications.

2 Experimental section

2.1 Materials

Nickel chloride hexahydrate ($NiCl_2·6H_2O$, AR), cobalt chloride hexahydrate ($CoCl_2·6H_2O$, AR), ammonium molybdate ($(NH_4)_2MoO_4$, AR), selenium dioxide (SeO_2, AR), choline chloride ($[HOC_2H_4N(CH_3)_3Cl]$, ChCl), glycol ($[(CH_2OH)_2]$, EG), and ethanol were purchased from Sinopharm chemical reagent Co., Ltd., Shanghai, China. Commercial Pt/C (Pt content was 20 wt.%) and Nafion solution were brought from commercial sources.

2.2 Synthesis of Re_{SA}-NiCoMo-Se

The Re_{SA}-NiCoMo-Se was fabricated by two-step electrodeposition. Firstly, the NiCoMo-Se was synthesized by electrodeposition using a CHI660e potentiostat (CH Instruments) in electrolyte containing 0.2 M $NiCl_2·6H_2O$, 0.1 M $CoCl_2·6H_2O$, 0.1 M $(NH_4)_2MoO_4$, and 0.2 g of SeO_2, where the electrolyte was obtained by mixing ChCl and EG with a molar ratio of 1:2 and stirring at 60 °C overnight (named as ethaline). The nickel foam (NF) substrate (1 cm × 2 cm) was washed by ultrasonic in turn for 30 min with 1.0 M HCl, ethanol, and deionized (DI) water, respectively. The NiCoMo-Se film was grown on NF substrate by chronoamperometry (CA) at −0.8 V (vs. Ag) for 1 h at 60 °C with a standard there-electrode system, employing NF, graphite rod, and non-aqueous Ag wire electrode as working, counter, and reference electrodes, respectively. The method for preparing NiCoMo contrast electrocatalyst was similar to synthesizing NiCoMo-Se without adding SeO_2 in electrolyte. Then, the Re_{SA}-NiCoMo-Se was obtained via the cyclic voltammetry (CV) from −0.6 to −1.2 V at 60 °C with a scan rate of 100 $mV·s^{-1}$ from 1000 to 4000 cycles. The three-electrode system consisted of the prepared NiCoMo-Se as working electrode, Re plate as counter electrode, non-aqueous Ag wire electrode as a reference electrode, and blank ethaline as electrolyte. All obtained samples were washed with ethanol and DI water and dried at 30 °C in vacuum. The fabrication process of enlarged Re_{SA}-NiCoMo-Se is listed in the Electronic Supplementary Material (ESM).

2.3 Characterization

The crystal structure and composition were determined by Smartlab X-ray diffraction (XRD) and grazing-incidence XRD (GIXRD), where the incidence angle was set to 1°. The morphology and elemental distribution were analyzed by scanning electron microscopy (SEM, FEI Nova Nano SEM 450), transmission electron microscopy (TEM, FEI Tecnai G2 F20 200), and high angle annular dark field-scanning transmission electron microscopy

(HAADF-STEM, FEI Theims Z) with 300 kV acceleration voltage. X-ray photoelectron spectroscopy (XPS) was recorded by Thermo SCIENTIFIC Nexsa, calibrated by the standard C 1s XPS peak (284.6 eV). Metal contents were measured by inductively coupled plasma-optical emission spectrometer (ICP-OES). The electron paramagnetic resonance (EPR) spectra were recorded on Bruker EMXplus at room temperature, dark environment, and atmospheric pressure. X-ray adsorption fine structure (XAFS) contains X-ray absorption near edge structure (XANES) and Fourier-transformed extended X-ray absorption fine structure (FT-EXAFS) measurements of Re L_3-edge were obtained at the Shanghai Synchrotron Radiation Facility (SSRF). The contact angle of H_2O was monitored by Theta Flex (Biolin Scientific).

2.4 Electrochemical measurement

The HER performances in 1.0 M KOH were tested by a Biologic-803 electrochemical station, where the synthesized catalysts, graphite rod, and Hg/HgO were used as working, counter, and reference electrodes, respectively. The linear sweep voltammetry (LSV) measurements were analyzed from −0.8 to −1.5 V (vs. Hg/HgO) at a scan rate of 2 mV·s^{-1} with 80% *iR*-compensation. The kinetic mechanism of the HER reaction was estimated by Tafel electrochemical equation $\eta = a + b\log j$ (where η is the overpotential, j is current density, a is the overpotential value when the current density is 1 A·cm^{-1}, and b is the Tafel slope). The detailed mass activities and turnover frequency (TOF) calculations of Re_{SA}-NiCoMo-Se and commercial Pt/C are listed in the ESM. The double-layer capacitance (C_{dl}) was performed by CV mode at a potential range of −0.4 to −0.5 V (vs. Hg/HgO) with different scan rates (20–120 mV·s^{-1}). The electrochemical impedance spectroscopy (EIS) was recorded to evaluate the charge transfer resistance (R_{ct}) from 1×10^5 to 10^{-1} Hz at −1.025 V (vs. Hg/HgO). The stability test was performed in CA mode at 500 and 1000 mA·cm^{-2} for 240 h. The AWE was conducted via SE300-AL (SCITECH KOREA) with polyphenylene sulfide (PPS) membrane (Agfa ZIRFON PERL). The polarization curves were tested from 1.3 to 2.5 V and the long-term stability test was performed at 2.0 V in 30 wt.% KOH solution at 70 °C.

2.5 Density theoretical calculation

The spin-polarized DFT calculations were finished by the Vienna *ab inito* simulation package (VASP) software [34, 35], which contained projected augmented wave (PAW) pseudo-potentials [36]. The exchange-correlation effects of energy were achieved by the generalized gradient approximation (GGA) method by using the Perdew–Burke–Ernzerhof (PBE) functional [37, 38]. The energy cutoff of plane wave expansions was set to 450 eV. The Monkhorst–Pack scheme with a *k*-point separate on length of 0.05 Å^{-1} was utilized for sampling the first Brillion zone [39], setting as 3 × 3 × 1. The vacuum space was adopted 15 Å above the molecular to separate periodic interactions during the whole calculations. The quasi-Newton l-BFGS method was used for geometry relaxation until the maximal energy and force on each degree of freedom were less than 1.0×10^{-5} eV and 0.01 eV·Å^{-1}, respectively. The initial Ni-$NiSe_2$ heterojunction was constructed by loading $NiSe_2$ onto the surface of Ni(111), which consisted of three layers of Ni metal atoms and two layers of $NiSe_2$ (168 Ni atoms and 48 Se atoms). The NiCoMo-Se model was created based on Ni-$NiSe_2$ by replacing ~ 8% and ~ 6% Ni atoms into Co and Mo atoms uniformly in all the layers (14 Co atoms, 10 Mo atoms, 144 Ni atoms, and 48 Se atoms). The Re_{SA}-NiCoMo-Se model was built by replacing surficial Ni into Re atoms on NiCoMo-Se model.

To obtain the free energy profile, Gibbs free energies for all the states were calculated based on the ZPE-corrected DFT total energy, which was set as the enthalpy at 0 K. It could be calculated with

$$G = H - TS = E_{DFT} + E_{ZPE} + \int_0^{298.15\,K} C_V \mathrm{d}T - TS \quad (1)$$

where G is the Gibbs free energy, H is the enthalpy, E_{DFT} is the total energy getting from DFT optimization, E_{ZPE} is the zero-point vibrational energy, C_V is the heat capacity, T is the kelvin temperature, and S is the entropy. The free energy for the gas-phase molecule was computed from thermodynamics by utilizing the standard thermodynamics data at the standard state.

3 Results and discussion

3.1 Morphological characterization of Re_{SA}-NiCoMo-Se

The target electrocatalyst, Re_{SA}-NiCoMo-Se heterostructure, was synthesized by a facile two-step electrodeposition process in ethaline (Fig. 1(a)). As shown in Figs. S1–S6 in the ESM, the NiCoMo-Se was electrodeposited on the bare NF at various voltages from −0.6 to −0.9 V in an ethaline-based electrolyte containing $NiCl_2{\cdot}6H_2O$, $CoCl_2{\cdot}6H_2O$, and $(NH_4)_2MoO_4$ as the metal sources, and SeO_2 as the selenium source. As the applied voltage and SeO_2 addition increased, the morphology of the as-synthesized NiCoMo-Se evolved from a globular structure to a sheet-like configuration. Specifically, the uniform nanosheets structural feature of NiCoMo-Se synthesized at −0.8 V with 0.2 g of SeO_2 addition contributes to expose edges and shorten the charge transport pathway for electrocatalytic reactions [40]. For comparison, a smooth metallic NiCoMo alloy film (named as NiCoMo) without SeO_2 addition was also prepared (Fig. S7 in the ESM), suggesting that SeO_2 (Se^{4+}) will be reduced and interacted with the Ni^{2+}, Co^{2+}, and Mo^{6+} in electrolyte to form an alloy-selenium compound [41]. Then, the Re_{SA}-NiCoMo-Se was synthesized by CV mode in blank ethaline electrolyte, where the bulk Re foil was selected as the counter electrode and the optimized NiCoMo-Se as the working electrode. After anchoring Re atoms, the Re_{SA}-NiCoMo-Se exhibits the fluffy structure, which facilitates sufficient contact with reactants and mass transfer (Figs. S8–S10 in the ESM). TEM, high-resolution TEM (HRTEM), and HAADF-STEM images further indicate that Re_{SA}-NiCoMo-Se is composed of the interconnected Co, Mo-doped $NiSe_2$, amorphous material, and NiCoMo alloy (Figs. 1(b)–1(d)). A lattice spacing of 0.209 nm pertains to the (111) crystal plane of face-centered cubic (fcc) NiCoMo alloy [42], and a lattice fringe with a lattice distance of 0.269 nm corresponds to the (210) of the plane of cubic $NiSe_2$. Disordered lattice fringes and broad diffraction rings in selected area electron diffraction (SAED) pattern combine to accurately illustrate the partial amorphous structure of Re_{SA}-NiCoMo-Se [43]. The formation of amorphous structures is probably due to the interference of Re atoms anchoring and the dissolution of support (Ni, Co, Mo, and Se, Table S2 in the ESM), leading to structural reconfiguration during the redox process by CV mode [44]. HAADF-STEM was further conducted to observe the atomic structure of Re_{SA}-NiCoMo-Se in detail. The atomic-level bright spots scattering throughout Re_{SA}-NiCoMo-Se marked with red circles were identified as individual Re atoms. The signal intensity profiles demonstrate the possible Re atoms dispersed on the $NiSe_2$

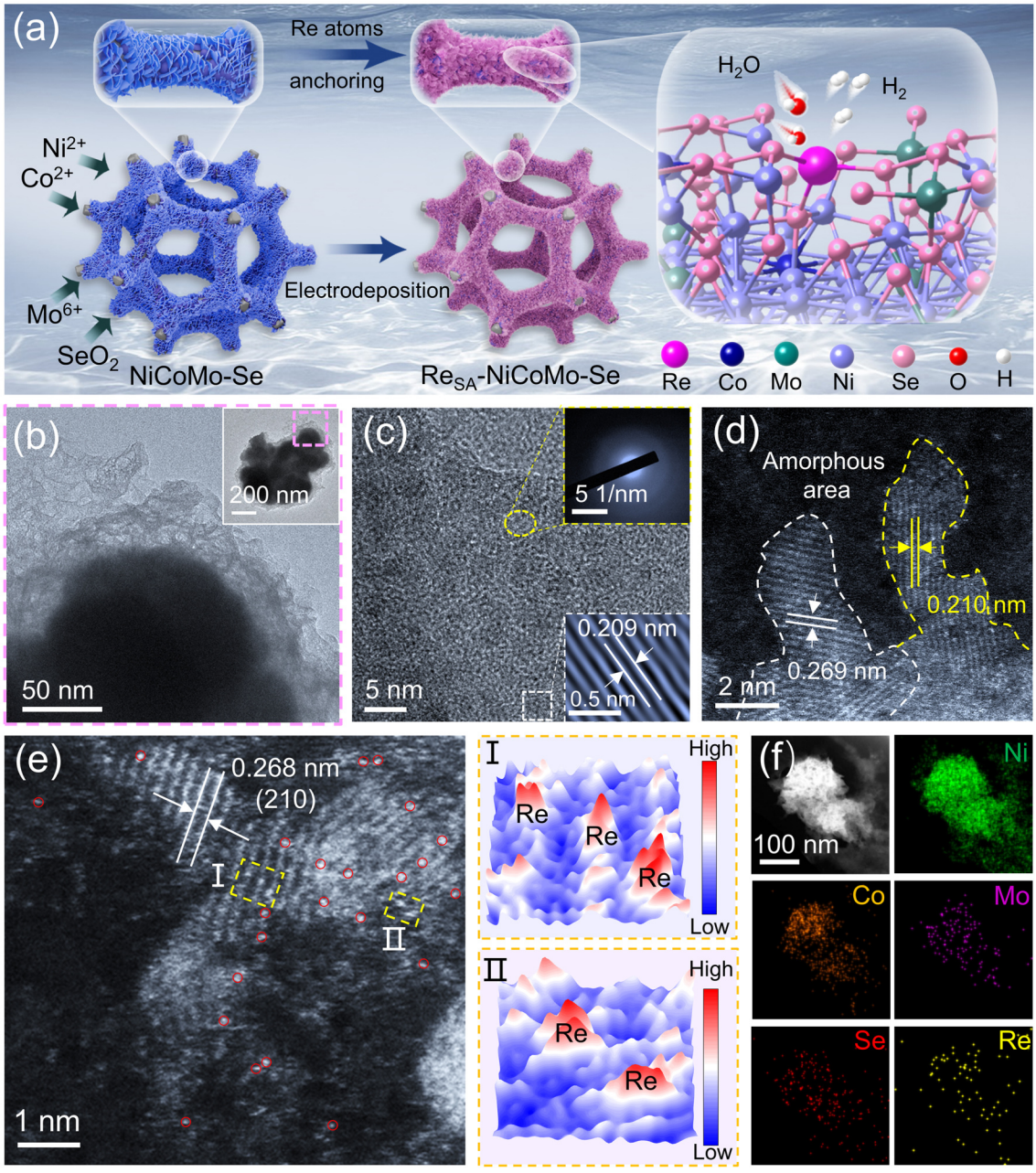

Figure 1 (a) Schematic illustration of the fabrication process for Re_{SA}-NiCoMo-Se and its application for HER in alkaline media. ((b) and (c)) TEM and HRTEM images of Re_{SA}-NiCoMo-Se. The insets show the SAED pattern and enlarged views of circled and framed area in (c), respectively. ((d) and (e)) HAADF-STEM images and corresponding plane intensity profiles labeled with yellow boxes of Re_{SA}-NiCoMo-Se. (f) Corresponding Ni, Co, Mo, Se, and Re elemental mappings of Re_{SA}-NiCoMo-Se.

and amorphous structure (Fig. 1(e)). In addition, the HAADF-STEM and corresponding elemental mapping images elucidate the homogenous distribution of Ni, Co, Mo, Se, and Re elements throughout the electrocatalyst (Fig. 1(f)).

3.2 Structural characterization of Re_{SA}-NiCoMo-Se

The XRD and GIXRD patterns of the as-obtained electrocatalysts were characterized to assure their crystal structures (Fig. 2(a), and Figs. S11 and S12 in the ESM). As for NiCoMo, the strong diffraction peaks located at 44.3°, 51.8°, and 76.3° represent lattices planes of (111), (200), and (220) for fcc structure, respectively, which can be index to metal Ni (JCPDS No. 004-0850). Besides, the diffraction peaks are shifted to smaller 2θ values compared with metal Ni reference, indicating that Mo and Co enter the Ni lattice to form NiCoMo alloy. Three small peaks appeared at around 29.9°, 33.5°, and 36.5° for NiCoMo-Se are ascribed to the standard profiles of the $NiSe_2$ (JCPDS No. 00-041-1495). It suggests that the addition of SeO_2 in the electrolyte enables the direct electrodeposition of a heterostructure comprising NiCoMo alloy and Co, Mo-doped $NiSe_2$. The intensity of diffraction peaks of $NiSe_2$ decreased in Re_{SA}-NiCoMo-Se, which is caused by the structural amorphization during the Re electrodeposition process, consistent with the catalyst synthesized using a graphite rod as counter electrode (Fig. S13(a) in the ESM). The chemical composition and electronic structure of NiCoMo, NiCoMo-Se, and Re_{SA}-NiCoMo-Se were investigated by XPS spectra. For Re_{SA}-NiCoMo-Se, the Ni 2p high-resolution

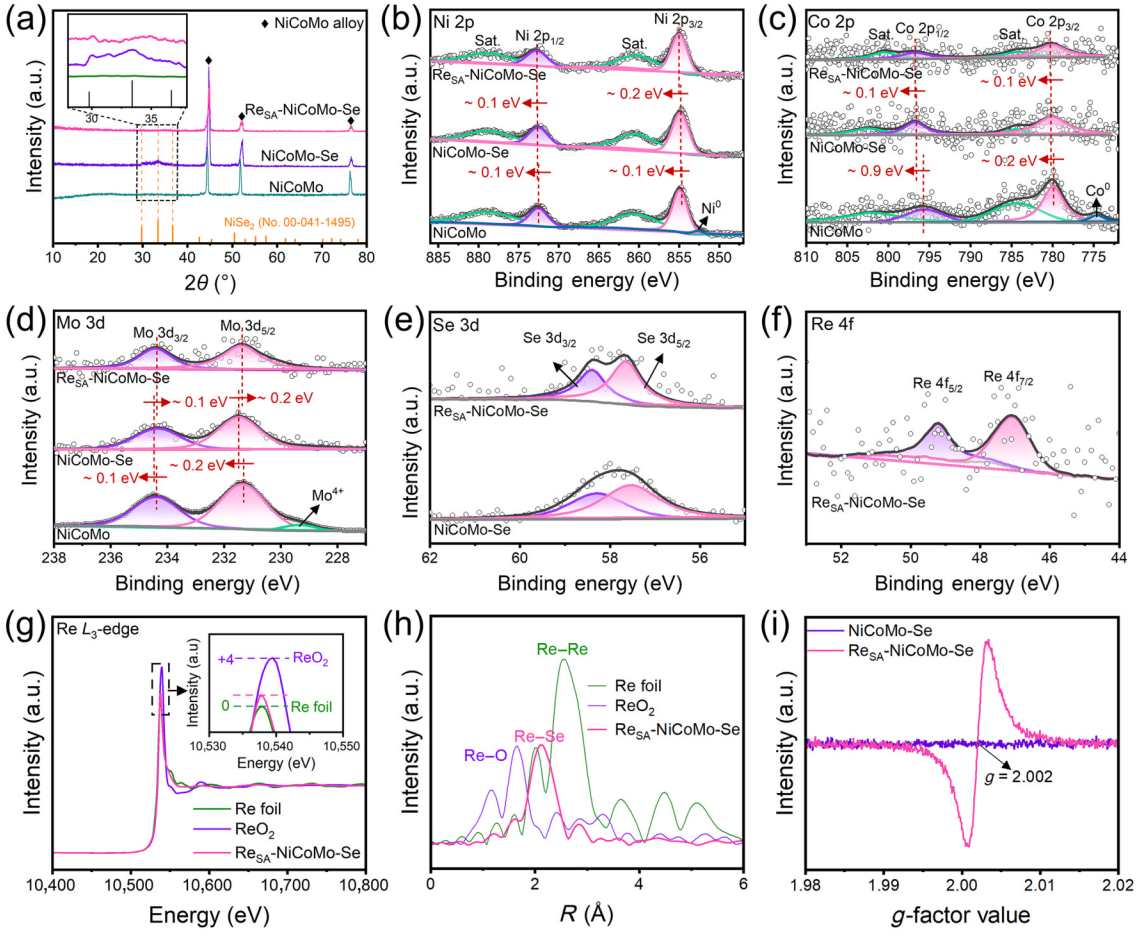

Figure 2 ((a)–(d)) The GIXRD patterns and high-resolution Ni 2p, Co 2p, and Mo 3d spectra of NiCoMo, NiCoMo-Se, and Re$_{SA}$-NiCoMo-Se. (e) The high-resolution Se 3d spectra of NiCoMo-Se and Re$_{SA}$-NiCoMo-Se. (f) The high-resolution Re 4f spectra of Re$_{SA}$-NiCoMo-Se. ((g) and (h)) The normalized XANES and FT-EXAFS spectra of Re L_3-edge for Re foil, ReO_2, and Re$_{SA}$-NiCoMo-Se. (i) The EPR spectra of NiCoMo-Se and Re$_{SA}$-NiCoMo-Se.

spectrum has two main peaks located at 872.7 and 855.0 eV assigned to Ni^{2+} in the Ni-Se for Ni 2p$_{1/2}$ and Ni 2p$_{3/2}$, respectively (Fig. 2(b)), while the Co 2p spectrum for Re$_{SA}$-NiCoMo-Se has two major peaks at binding energies of 796.7 and 780.3 eV attributed to Co 2p$_{1/2}$ and Co 2p$_{3/2}$, respectively (Fig. 2(c)). Besides, the peaks at 852.8 and 774.5 eV correspond to metallic Ni and Co species derived from NiCoMo alloy, respectively. Remarkably, the binding energies of Ni 2p and Co 2p in NiCoMo-Se show positive shift relative to NiCoMo, due to strong interfacial electronic interaction in NiCoMo alloy/Co, Mo-doped $NiSe_2$ heterostructure [40]. Upon the successful introduction of Re single atoms, a further positive shift in these binding energies is observed, suggesting an adjustment in the electronic structure that strengthens the interaction between Re metal single atoms and Co, Mo-doped $NiSe_2$ support [45]. In Fig. 2(d), Mo 3d spectrum of Re$_{SA}$-NiCoMo-Se displays a conspicuous doublet located at 234.3 and 231.3 eV corresponding to Mo 3d$_{3/2}$ and Mo 3d$_{5/2}$, respectively, illustrating a downshift of ~ 0.1 eV in comparison to NiCoMo-Se, indicating that the introduction of Re atoms arises the electronic accumulation region around Mo atoms [46]. The peaks at 58.4 and 57.6 eV represent Se 3d$_{3/2}$ and Se 3d$_{5/2}$ for Re$_{SA}$-NiCoMo-Se, respectively, suggesting the formation of a metal–selenium bond (Fig. 2(e)). Meanwhile, the Re 4f XPS spectrum of Re$_{SA}$-NiCoMo-Se exhibited Re 4f$_{5/2}$ and Re 4f$_{7/2}$ oxidation states (Fig. 2(f)).

To further verify the electronic state and local coordination environment of the Re atoms in Re$_{SA}$-NiCoMo-Se, XANES and FT-EXAFS were further performed. In Re L_3-edge XANES spectra (Fig. 2(g)), the intensity of the white line peak for Re$_{SA}$-NiCoMo-Se is higher than that of the Re foil but lower than that of the standard ReO_2, suggesting that the isolated Re atom has a valence between Re^0 (Re foil) and Re^{4+} (ReO_2), agreeing with the XPS results [19]. The k^3-weighted Re L_3-edge FT-EXAFS spectra (Fig. 2(h)) showed that the peak at 2.12 Å was attributed to the first Re–Se shell in the spectrum of Re$_{SA}$-NiCoMo-Se. In comparison, the absence of a scattering peak at about 2.55 Å, derived from Re–Re bond in the spectrum of Re foil, indicated the existence of the Re individual atoms rather than Re clusters [16]. Additionally, the FT-EXAFS fitting results (Fig. S15 and Table S1 in the ESM) revealed the average coordination number about the central Re atoms to be 5.1 with a bond length of 2.49 Å for the Re–Se scattering path, implying that the Re species likely substitutes for Ni sites and bonds to the support surface with the presence of Se vacancies in its vicinity [23]. Meanwhile, the EPR investigations were also applied to verify the existence of Se vacancies in Re$_{SA}$-NiCoMo-Se (Fig. 2(i) and Fig. S16 in the ESM). The EPR signal at g = 2.002 for Re$_{SA}$-NiCoMo-Se is caused by the trapped electrons from the Se vacancies [47], while no obvious signal can be observed for the NiCoMo-Se at the same position, demonstrating that abundant Se vacancies have been successfully incorporated into Re$_{SA}$-NiCoMo-Se during the electrodepositing process. Based on the morphology

and structure characterization results, it can be revealed that the heterostructure combined Re single-atoms anchored Co, Mo-doped $NiSe_2$ with NiCoMo alloy was synthesized successfully by two-step electrodeposition in ethaline.

3.3 Electrocatalytic activity analysis of Re_{SA}-NiCoMo-Se

The electrocatalytic HER performances of the different synthesized electrocatalysts were evaluated using a standard three-electrode system in 1 M KOH solution. After rigorous HER performance comparisons, the electrodeposition voltage of −0.8 V and SeO_2 addition of 0.2 g were chosen as the optimal conditions for NiCoMo-Se synthesis (Fig. S17 in the ESM). Besides, after 3000 cycles of Re deposition, the catalyst with 0.04 wt.% Re content shows the best HER performance (Figs. S18–S20 in the ESM). As shown in Fig. 3(a), the polarization curves exhibit that Re_{SA}-NiCoMo-Se just needs an overpotential of 23 mV to achieve 10 mA·cm^{-2}, which is lower than that of NiCoMo-Se (44 mV), NiCoMo (135 mV), and commercial Pt/C (95 mV), indicating that the introduction of Re single-atoms is essential to enhance the HER activity. At the current densities of 100, 500, and 1000 mA·cm^{-2}, the

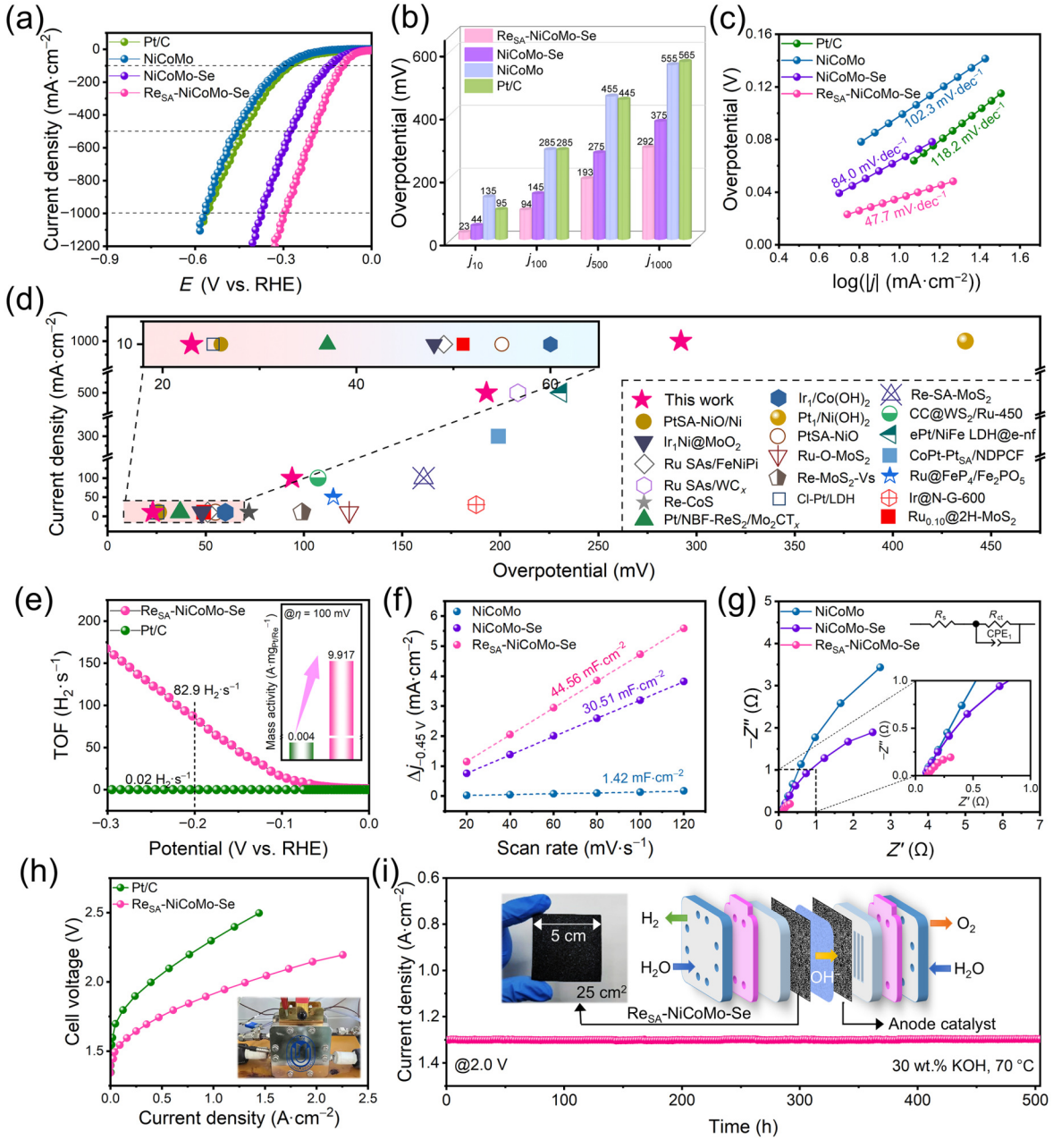

Figure 3 (a) Polarization curves of Re_{SA}-NiCoMo-Se, NiCoMo-Se, NiCoMo, and commercial Pt/C. (b) Comparison of overpotentials required to achieve 10, 100, 500, and 1000 mA·cm^{-2} for various catalysts. (c) Tafel plots of Re_{SA}-NiCoMo-Se and other catalysts obtained from the corresponding polarization curves. (d) Comparison of overpotentials at different current densities of reported Pt, Ru, Ir, and Re single-atoms HER electrocatalysts. (e) TOF curves and mass activity values at overpotential of 100 mV of Re_{SA}-NiCoMo-Se and commercial Pt/C. (f) Linear fitting of the capacitive currents against scan rate at a potential of −0.45 V (vs. Hg/HgO) for NiCoMo, NiCoMo-Se, and Re_{SA}-NiCoMo-Se. (g) EIS Nyquist plots of NiCoMo, NiCoMo-Se, and Re_{SA}-NiCoMo-Se. (h) Polarization curves of Re_{SA}-NiCoMo-Se and commercial Pt/C measured in AWE. The inset is the photograph of AWE under working conditions. (i) Stability test of Re_{SA}-NiCoMo-Se in the AWE at 2.0 V. The insets are photograph of enlarged Re_{SA}-NiCoMo-Se electrode (25 cm^2) and schematic diagram of AWE device.

overpotentials of Re_{SA}-NiCoMo-Se were 94, 193, and 292 mV, respectively, disclosing that Re_{SA}-NiCoMo-Se could meet the demand for industrial applications (Fig. 3(b)). It is obvious that the fitting values of Tafel slopes for Re_{SA}-NiCoMo-Se, NiCoMo-Se, NiCoMo, and Pt/C correspond to 47.7, 84.0, 102.3, and 118.2 mV·dec^{-1}, respectively (Fig. 3(c)). Based on the analysis of the Tafel slopes, Re_{SA}-NiCoMo-Se involves a Volmer–Heyrovsky mechanism during HER, indicating that the incorporation of Re single atoms enhances reaction kinetics by shifting the rate-determining step from water adsorption and dissociation (NiCoMo-Se) to electrochemical desorption, thereby optimizing the desorption capacity of *H [48]. Compared to most of the reported start-of-the-art Pt-, Ir-, Ru-, and Re-single-atom HER electrocatalysts, the Re_{SA}-NiCoMo-Se is superior at various current densities (Fig. 3(d) and Table S3 in the ESM). Furthermore, TOF was further calculated to evaluate the intrinsic per-site activity of Re single atoms for revealing the intrinsic catalytic behavior [49]. In Fig. 3(e), the Re_{SA}-NiCoMo-Se can supply 82.9 H_2·s^{-1} at the overpotential of 200 mV, far higher than commercial Pt/C (0.02 H_2·s^{-1}). Besides, the superb activity of the Re_{SA}-NiCoMo-Se is likewise evidenced by its mass activity [50], eliminating the influence of the NiCoMo-Se catalytic support, where the Re single atoms still exhibits excellent intrinsic HER electrocatalytic performance (9.917 A·mg$_{Re}^{-1}$, inset in Fig 3(e)). The C_{dl} is applied to estimate the electrochemically active surface area (ECSA) of electrocatalysts [51, 52]. The C_{dl} for NiCoMo was found to be 1.42 mF·cm^{-2}, which increased to 30.51 mF·cm^{-2} after adding SeO_2 and further to 44.56 mF·cm^{-2} following Re single atoms electrodeposition (Fig. 3(f) and Fig. S21 in the ESM). Besides, the Re_{SA}-NiCoMo-Se possesses the largest ECSA value of 1114 cm^2, which is higher than that of NiCoMo-Se (762.8 cm^2) and NiCoMo (35.5 cm^2). It indicates that the Re_{SA}-NiCoMo-Se has a larger ESCA, providing more catalytic sites to enhance the reaction rate attributed to the fluffy morphology and the amorphous structural characteristics of electrocatalyst [43]. EIS was employed to provide further insight into the electrical conductivity of studied electrocatalysts for basic HER (Fig. 3(g) and Table S4 in the ESM) [53, 54], and Re_{SA}-NiCoMo-Se with the smallest R_{ct} exhibits the fastest interfacial charge transfer rate compared to other catalysts during alkali hydrogen evolution. The H_2O contact angles on the surface of the NiCoMo and NiCoMo-Se in the air were 105.2° and 48.2°, whereas that for Re_{SA}-NiCoMo-Se was 0° (Fig. S22 in the ESM). The modification of the amorphous surface markedly enhances the affinity of Re_{SA}-NiCoMo-Se for H_2O, transitioning it from a predominantly hydrophobic state (NiCoMo and NiCoMo-Se) to a distinctly superhydrophilic state, which not only manipulated the wettability of the surface but also preserved its structural integrity [55].

Additionally, to meet industrial requirements, it is essential to measure the long-term stability of Re_{SA}-NiCoMo-Se. The Re_{SA}-NiCoMo-Se can be well maintained for at least 10 days (240 h) with slight degradation of 99.1% at 500 mA·cm^{-2} and 94.7% at 1000 mA·cm^{-2} (Fig. S23 in the ESM), showing tremendous stability under large current densities, which may be applied in industrial water splitting in the future. XRD pattern, SEM images, and XPS spectra suggested that the structure and morphology of Re_{SA}-NiCoMo-Se showed slightly change after the electrochemical stability test, further supporting the remarkable structural stability of the catalyst (Figs. S24 and S25 in the ESM). The AWE device was employed to further evaluate the practical potential of electrocatalysts. The commercial $NiFeO_x$ loaded nickel fiber paper as an anode was assembled with Re_{SA}-NiCoMo-Se (25 cm^2, Fig. S26 in the EMS) and operated in 30 wt.% KOH solution under 70 °C. The industrial-scale current density of 1000 mA·cm^{-2} was achieved at only 1.91 V_{cell}, which is superior to Pt/C||$NiFeO_x$ system (2.31 V_{cell}, Fig. 3(h)). In addition, the Re_{SA}-NiCoMo-Se||$NiFeO_x$ system also exhibits excellent stability of 500 h of durable and stable operation at 2.0 V_{cell} with only slight decay (Fig. 3(i)). The good durability of the Re_{SA}-NiCoMo-Se was confirmed by HAADF-STEM, XAFS, and ICP-OES analyses (Figs. S27 and S28, and Tables S1 and S2 in the ESM). The high stability of Re_{SA}-NiCoMo-Se primarily stems from the reinforced Re–Se bonding, which secures the active sites, synergized with the protective and stable NiCoMo-Se support architecture that effectively mitigates overall electrocatalytic performance degradation. These merits confirm the advanced and reliable potential of Re_{SA}-NiCoMo-Se electrocatalyst for practical industrial-scale water electrolysis.

3.4 DFT analysis

The HER underlying mechanism of Re_{SA}-NiCoMo-Se was further investigated by DFT calculations. For comparison, the NiCoMo-Se, consisting of a NiCoMo alloy and Co,Mo-doped $NiSe_2$, and the ReSA-NiCoMo-Se, consisting of a single Re atom replacing a surface Ni atom of the Co,Mo-doped $NiSe_2$ and the NiCoMo alloy, were modeled based on the XRD, ICP-OES, and FT-EXAFS results (Fig. S29 in the ESM). Figure 4(a) shows that there is an obvious charge transfer at the interface between NiCoMo alloy and Co, Mo-doped $NiSe_2$. After immobilizing Re atoms, the charge accumulation is distributed around the Re site to form a located electron-rich region (Fig. 4(b)), suggesting that Re single atom coupled with NiCoMo-Se heterostructure could possess more free electrons to promote the adsorbed H conversion and H_2 evolution on Re sites [56]. The density of states (DOS, Fig. 4(c)) of Re_{SA}-NiCoMo-Se shows higher occupation than that of the NiCoMo-Se near the Fermi level, indicating their enhanced electron mobility and higher intrinsic electrical conductivity (Fig. S30 in the ESM) [29]. This indicates that the atomic Re dopant could effectively optimize the d-electron domination of Mo atoms, thus leading to enhanced catalytic activity. Notably, the strong affinity enables the intermediates difficult to desorb, thus against the electrocatalytic reaction kinetics. The high H_2O dissociation barrier may hamper the decomposition of H_2O into *H species and result in sluggish HER kinetics [57]. As shown in Fig. 4(d), NiCoMo-Se has large water adsorption energy value of −0.89 eV at Co site. In contrast, the ΔE_{*H_2O} at Co site of the Re_{SA}-NiCoMo-Se decreases and the Ni site serves as the primary water adsorption sites, suggesting that the sluggish Volmer process can be greatly accelerated after the introduction of atomic-level Re dopant. The calculated hydrogen adsorption free energy in Fig. 4(e) shows a moderate ΔG_{*H} value of 0.206 eV for Re_{SA}-NiCoMo-Se, which is lower than that of NiCoMo-Se (0.283 eV). These results indicate that the Re sites are active sites for HER on Re_{SA}-NiCoMo-Se, and the proceeding of H_2O dissociation on Re_{SA}-NiCoMo-Se is easier than on NiCoMo-Se (Fig. 4(f), and Figs. S31 and S32 in the ESM). Therefore, the exceptional HER performance of Re_{SA}-NiCoMo-Se stems from a triple synergy between its atomic, electronic, and morphological structures: (i) The homogeneous multi-element composition creates synergistic catalytic support and stabilizes the Re active sites. (ii) Atomically dispersed Re atoms modulate the electronic structure of the host NiCoMo-Se matrix, optimizing H_2O dissociation and ΔG_{*H}. (iii) The three-dimensional floss-like

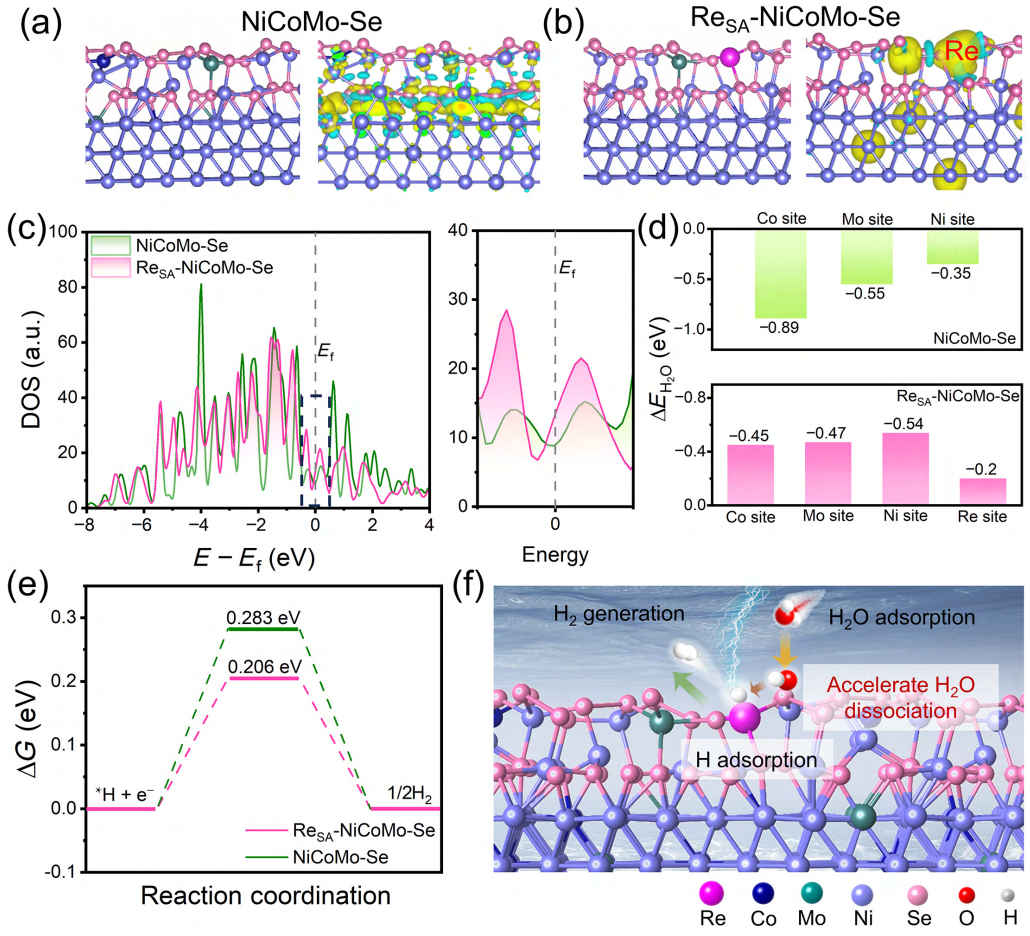

Figure 4 ((a) and (b)) The optimized configuration and differential charge density distribution of NiCoMo-Se and Re$_{SA}$-NiCoMo-Se. The yellow and green areas represent electron accumulation and depletion, respectively. (c) Calculated density of states for NiCoMo-Se and Re$_{SA}$-NiCoMo-Se. (d) Adsorption energy values of H_2O at different sites on NiCoMo-Se and Re$_{SA}$-NiCoMo-Se. (e) Calculated hydrogen adsorption Gibbs free energy diagrams of NiCoMo-Se and Re$_{SA}$-NiCoMo-Se. (f) The mechanism illustration of electrocatalytic HER under alkaline media, including water activation, *H intermediate formation, and hydrogen generation on Re$_{SA}$-NiCoMo-Se.

architecture provides a large electrochemical surface area and facilitates mass/charge transport. This integrated structure collectively enhances intrinsic activity, increases active site density, and improves reaction kinetics.

4 Conclusions

In conclusion, we developed a Re-incorporated Co, Mo-doped $NiSe_2$/NiCoMo heterostructure electrocatalyst via a controlled electrodeposition in a deep eutectic solvent. The optimized Re$_{SA}$-NiCoMo-Se catalyst demonstrates an ultralow overpotentials of 23 and 292 mV at 10 and 1000 mA·cm^{-2}, respectively, while exhibits excellent stability under large current density. Meanwhile, the flowing alkaline water electrolyzer confirms the catalyst could deliver 1000 mA·cm^{-2} at 1.91 V and exhibit over 500 h of durability at 2.0 V without obvious decay. DFT results reveal that single-atom Re acted as a catalytic site, effectively accelerating the water dissociation and optimizing hydrogen adsorption energy enabled by atomic-level modulation the electronic structure and coordination environment of host material. This research underscores the electrochemical synthesis of Re single-atom materials and their potential as effective, durable, and scalable electrocatalysts for industrial hydrogen production. Future research would focus on extending the synthetic strategy, testing in industrially relevant electrolyzer setups, conducting techno-economic analysis, etc.

Electronic Supplementary Material: Supplementary material (mass activities and TOF calculation details, SEM, TEM, XRD, EXAFS fitting parameters, additional electrochemical measurements, contact angles, morphology and structure characterizations after stability test, DOS, *OH adsorption energy, elemental contents, and comparison of the HER performance) is available in the online version of this article at https://doi.org/10.26599/NR.2026.94908569.

Data availability

All data needed to support the conclusions in the paper are presented in the manuscript and the Electronic Supplementary Material. Additional data related to this paper may be requested from the corresponding author upon request.

Acknowledgements

The authors thank the National Natural Science Foundation of China (Nos. 52374307, 52022054, 52204317, 52334009, and 62474047), the National Key Research and Development Program

of China (No. 2022YFC2906100), the Shanghai Leading Talent Program of Eastern Talent Plan (No. LJ2025029), and the Innovation Program of Shanghai Municipal Education Commission (No. 2023ZKZD48).

Declaration of competing interest

All the contributing authors report no conflict of interests in this work.

Author contribution statement

X. W. X.: Conceptualization, methodology, formal analysis, writing – original draft. X. Q. Z.: Formal analysis, data curation. N. N. Z.: Methodology. X. Y. (Xin Yuan): Data curation. Y. F. M.: Methodology. S. J. W.: Supervision, writing – review & editing. Y. G.: Investigation. Z. Y. P.: Data curation. X. Y. (Xing Yu): Data curation. G. S. L.: Formal analysis. S. H.: Formal analysis. L. J.: Supervision. X. G. L.: Supervision, funding acquisition. X. L. Z.: Writing – review & editing, conceptualization, funding acquisition. All the authors have approved the final manuscript.

Use of AI statement

None.

References

[1] Shih, A. J.; Monteiro, M. C. O.; Dattila, F.; Pavesi, D.; Philips, M.; da Silva, A. H. M.; Vos, R. E.; Ojha, K.; Park, S.; van der Heijden, O. et al. Water electrolysis. *Nat. Rev. Methods Primers* **2022**, *2*, 84.

[2] Chatenet, M.; Pollet, B. G.; Dekel, D. R.; Dionigi, F.; Deseure, J.; Millet, P.; Braatz, R. D.; Bazant, M. Z.; Eikerling, M.; Staffell, I. et al. Water electrolysis: From textbook knowledge to the latest scientific strategies and industrial developments. *Chem. Soc. Rev.* **2022**, *51*, 4583–4762.

[3] Cui, W. G.; Gao, F.; Na, G. Q.; Wang, X. Q.; Li, Z. L.; Yang, Y. X.; Niu, Z. Q.; Qu, Y. Q.; Wang, D. S.; Pan, H. G. Insights into the pH effect on hydrogen electrocatalysis. *Chem. Soc. Rev.* **2024**, *53*, 10253–10311.

[4] Wang, C. X.; Guo, W. X.; Chen, T. L.; Lu, W. Y.; Song, Z. Y.; Yan, C. C.; Feng, Y.; Gao, F. M.; Zhang, X. N.; Rao, Y. P. et al. Advanced noble-metal/transition-metal/metal-free electrocatalysts for hydrogen evolution reaction in water-electrolysis for hydrogen production. *Coord. Chem. Rev.* **2024**, *514*, 215899.

[5] Gao, G. L.; Zhao, G. Z.; Zhu, G.; Sun, B. W.; Sun, Z. X.; Li, S. L.; Lan, Y. Q. Recent advancements in noble-metal electrocatalysts for alkaline hydrogen evolution reaction. *Chin. Chem. Lett.* **2025**, *36*, 109557.

[6] Seh, Z. W.; Kibsgaard, J.; Dickens, C. F.; Chorkendorff, I.; Nørskov, J. K.; Jaramillo, T. F. Combining theory and experiment in electrocatalysis: Insights into materials design. *Science* **2017**, *355*, eaad4998.

[7] Kim, J.; Oh, J.; Baskaran, S.; Kim, T. G.; Kim, S.; Yang, J.; Jung, J.; Yoon, S. M. Rhenium redefined as electrocatalyst: Hydrogen evolution efficiency boost via Pt and Ni doping. *Appl. Catal. B: Environ. Energy* **2024**, *347*, 123791.

[8] U.S. Geological Survey. *Mineral Commodity Summaries 2025*; U.S. Geological Survey: Reston, 2025; pp 212.

[9] Ramírez, A. M. R.; Heidari, S. M.; Vergara, A.; Aguilera, M. V.; Preuss, P.; Camarada, M. B.; Fischer, A. Rhenium-based electrocatalysts for water splitting. *ACS Mater. Au* **2023**, *3*, 177–200.

[10] Kirillov, E.; Bochkareva, Z.; Semenishchev, V.; Kirillov, S.; Bunkov, G.; Rychkov, V. Anion exchange recovery of rhenium from industrial liquors followed by direct synthesis of a rhenium halide salt. *Hydrometallurgy* **2024**, *230*, 106387.

[11] Méndez, E.; Cerdá, M. F.; Castro Luna, A. M.; Zinola, C. F.; Kremer, C.; Martins, M. E. Electrochemical behavior of aqueous acid perrhenate-containing solutions on noble metals: Critical review and new experimental evidence. *J. Colloid Interface Sci.* **2003**, *263*, 119–132.

[12] Cao, H. Z.; Chai, D. G.; Wu, L. K.; Zheng, G. Q. Communication-A mechanistic study on electrodeposition of rhenium from acidic solution of ammonium perrhenate. *J. Electrochem. Soc* **2017**, *164*, D825–D827.

[13] Hahn, B. P.; May, R. A.; Stevenson, K. J. Electrochemical deposition and characterization of mixed-valent rhenium oxide films prepared from a perrhenate solution. *Langmuir* **2007**, *23*, 10837–10845.

[14] Rivera, J. G.; Garcia-Garcia, R.; Coutino-Gonzalez, E.; Orozco, G. Hydrogen evolution reaction on metallic rhenium in acid media with or without methanol. *Int. J. Hydrogen Energy* **2019**, *44*, 27472–27482.

[15] Garcia-Garcia, R.; Ortega-Zarzosa, G.; Rincón, M. E.; Orozco, G. The hydrogen evolution reaction on rhenium metallic electrodes: A selected review and new experimental evidence. *Electrocatalysis* **2015**, *6*, 263–273.

[16] Shen, C. Y.; Meng, X. Y.; Zou, R.; Sun, K. H.; Wu, Q. L.; Pan, Y. X.; Liu, C. J. Boosted sacrificial-agent-free selective photoreduction of CO_2 to CH_3OH by rhenium atomically dispersed on indium oxide. *Angew. Chem., Int. Ed.* **2024**, *63*, e202402369.

[17] Luo, S. C.; Xu, B. R.; Tan, D. L.; Hua, W. B.; Yan, G. C.; Lin, B.; Yang, G. D. Frustrated lewis-pair catalyst based on Re single atoms for efficient solar-driven CO_2 conversion. *ACS Catal.* **2025**, *15*, 7518–7529.

[18] Shen, C. Y.; Sun, K. H.; Zou, R.; Wu, Q. L.; Mei, D. H.; Liu, C. J. CO_2 hydrogenation to methanol on indium oxide-supported rhenium catalysts: The effects of size. *ACS Catal.* **2022**, *12*, 12658–12669.

[19] Yue, X. Z.; Liu, Y. C.; Lu, B. A.; Du, X.; Lei, W.; Liu, Z. Y.; Yi, S. S.; Lu, C. Inherent anti-Fenton property of single-atom rhenium for the ultra-durable oxygen reduction reaction. *Energy Environ. Sci.* **2024**, *17*, 5892–5900.

[20] Zhang, X. H.; Shang, L.; Yang, Z. J.; Zhang, T. R. A rhenium single-atom catalyst for the electrocatalytic oxygen reduction reaction. *ChemPlusChem* **2021**, *86*, 1635–1639.

[21] Jiang, X. Z.; Wu, X. H.; Lv, M. Y.; Pan, X. L.; Wang, H.; Li, C. Y.; Chen, M. X.; Chen, W.; Zhang, B.; Yu, G. T. et al. "Suspended" single rhenium atoms on nickel oxide for efficient electrochemical oxidation of glucose. *J. Am. Chem. Soc.* **2025**, *147*, 4886–4895.

[22] Yu, J. M.; Qian, Y. T.; Wang, Q.; Su, C. L.; Lee, H.; Shang, L.; Zhang, T. R. Single-atomic rhenium-assisted 2H-to-1T phase transformation of MoS_2 nanosheets boosting electrocatalytic hydrogen evolution. *EES Catal.* **2023**, *1*, 571–579.

[23] Zhang, Y. J.; Wang, X. K.; Song, X. J.; Jiang, H. Q. Collaborative effect between single-atom Re and S vacancy on modulating localized electronic structure of MoS_2 catalysts for alkaline hydrogen evolution. *Nano Res.* **2024**, *17*, 9507–9517.

[24] Yu, J. M.; Qian, Y. T.; Seo, S.; Tran, N. Q.; Shao, X. D.; Liu, Y.; Lee, J. S.; Le, T. A.; Lee, H.; Peng, L. S. Electronic structure engineering of CoS catalysts by rhenium modification for efficient alkaline hydrogen evolution. *Rare Met.* **2025**, *44*, 7349–7359.

[25] Hussain, I.; Sahoo, S.; Lamiel, C.; Nguyen, T. T.; Ahmed, M.; Xi, C.; Iqbal, S.; Ali, A.; Abbas, N.; Javed, M. S. et al. Research progress and future aspects: Metal selenides as effective electrodes. *Energy Storage Mater.* **2022**, *47*, 13–43.

[26] Luo, Z. K.; Tong, L. Z.; Lin, Z. P.; Amin, R. S.; Ren, J. N.; El-Khatib, K. M.; Wang, C. Ferrum-doped nickel selenide@tri-nickel diselenide heterostructure electrocatalysts with efficient and stable water splitting for hydrogen and oxygen production. *Adv. Compos. Hybrid Mater.* **2023**, *6*, 159.

[27] Jiang, F.; Wang, Y. C.; Peng, H. Y.; Wu, Y. Q.; Zhang, Z. Y.; Li, Y. C.; Zhong, S. C.; Chen, X. B.; Li, J. Q.; Wang, Y. et al. Triggering

asymmetric hybridization via Ni–Se–Co electron bridges on rich amorphous heterostructured nickel selenide for durable alkaline water splitting. *Appl. Catal. B: Environ. Energy* **2025**, *372*, 125326.

[28] Xu, J. C.; Ruan, J. X.; Jian, Y. Q.; Lao, J. Y.; Li, Z. L.; Xie, F. Y.; Jin, Y. S.; Yu, X.; Lee, M. H.; Wang, Z. Y. et al. Cobalt-doping induced formation of five-coordinated nickel selenide for enhanced ethanol assisted overall water splitting. *Small* **2024**, *20*, 2305905.

[29] Jiang, K.; Liu, B. Y.; Luo, M.; Ning, S. C.; Peng, M.; Zhao, Y.; Lu, Y. R.; Chan, T. S.; de Groot, F. M. F.; Tan, Y. W. Single platinum atoms embedded in nanoporous cobalt selenide as electrocatalyst for accelerating hydrogen evolution reaction. *Nat. Commun.* **2019**, *10*, 1743.

[30] Zhou, K. L.; Wang, Z. L.; Han, C. B.; Ke, X. X.; Wang, C. H.; Jin, Y. H.; Zhang, Q. Q.; Liu, J. B.; Wang, H.; Yan, H. Platinum single-atom catalyst coupled with transition metal/metal oxide heterostructure for accelerating alkaline hydrogen evolution reaction. *Nat. Commun.* **2021**, *12*, 3783.

[31] Zhang, J. Q.; Zhao, Y. F.; Guo, X.; Chen, C.; Dong, C. L.; Liu, R. S.; Han, C. P.; Li, Y. D.; Gogotsi, Y.; Wang, G. X. Single platinum atoms immobilized on an MXene as an efficient catalyst for the hydrogen evolution reaction. *Nat. Catal.* **2018**, *1*, 985–992.

[32] Wang, S. J.; Lu, M. H.; Xia, X. W.; Wang, F.; Xiong, X. L.; Ding, K.; Pang, Z. Y.; Li, G. S.; Xu, Q.; Hsu, H. Y. et al. A universal and scalable transformation of bulk metals into single-atom catalysts in ionic liquids. *Proc. Natl. Acad. Sci. USA* **2024**, *121*, e2319136121.

[33] Huang, Q.; Lyons, T. W. Electrodeposition of rhenium with suppressed hydrogen evolution from water-in-salt electrolyte. *Electrochem. Commun.* **2018**, *93*, 53–56.

[34] Kresse, G.; Hafner, J. *Ab initio* molecular dynamics for liquid metals. *Phys. Rev. B* **1993**, *47*, 558–561.

[35] Kresse, G.; Hafner, J. *Ab initio* molecular-dynamics simulation of the liquid-metal-amorphous-semiconductor transition in germanium. *Phys. Rev. B* **1994**, *49*, 14251–14269.

[36] Blöchl, P. E. Projector augmented-wave method. *Phys. Rev. B* **1994**, *50*, 17953–17979.

[37] Kresse, G.; Joubert, D. From ultrasoft pseudopotentials to the projector augmented-wave method. *Phys. Rev. B* **1999**, *59*, 1758–1775.

[38] Perdew, J. P.; Burke, K.; Ernzerhof, M. Generalized gradient approximation made simple. *Phys. Rev. Lett.* **1996**, *77*, 3865–3868.

[39] Monkhorst, H. J.; Pack, J. D. Special points for Brillouin-zone integrations. *Phys. Rev. B* **1976**, *13*, 5188–5192.

[40] Xia, X. W.; Wang, S. J.; Liu, D.; Wang, F.; Zhang, X. Q.; Zhang, H.; Yu, X.; Pang, Z. Y.; Li, G. S.; Chen, C. Y. et al. Electronic modulation in Cu doped NiCo LDH/NiCo heterostructure for highly efficient overall water splitting. *Small* **2024**, *20*, 2311182.

[41] Anicai, L.; Sin, I.; Brincoveanu, O.; Costovici, S.; Cotarta, A.; Cojocaru, A.; Enachescu, M.; Visan, T. Electrodeposition of lead selenide films from ionic liquids based on choline chloride. *Appl. Surf. Sci.* **2019**, *475*, 803–812.

[42] Shi, G. Y.; Tano, T.; Iwataki, T.; Tryk, D. A.; Uchida, M.; Iiyama, A.; Terao, K.; Tamoto, K.; Yamaguchi, M.; Miyatake, K. et al. Highly active nanostructured NiCoMo-based catalyst for oxygen evolution in anion-exchange membrane water electrolysis. *ACS Appl. Energy Mater.* **2023**, *6*, 10742–10747.

[43] Shi, Y.; Zhou, S. L.; Liu, J. X.; Zhang, X.; Yin, J.; Zhan, T. R.; Yang, Y.; Li, G. J.; Lai, J. P.; Wang, L. An integrated amorphous cobalt phosphoselenide electrocatalyst with high mass activity boosts alkaline overall water splitting. *Appl. Catal. B: Environ.* **2024**, *341*, 123326.

[44] Yu, J.; Li, X. Y.; Zhang, Q.; Li, W. L.; Zhou, M.; Zhang, Y. H.; Xiao, P. Amorphous/crystalline hetero-phase Ni-doped Co/CoP: Cyclic voltammetry synthesis and energy-efficient hydrazine‑assisted water splitting via N–N breakage. *Appl. Catal. B: Environ. Energy* **2025**, *373*, 125374.

[45] Shah, K.; Dai, R. Y.; Mateen, M.; Hassan, Z.; Zhuang, Z. W.; Liu, C. H.; Israr, M.; Cheong, W. C.; Hu, B. T.; Tu, R. Y. et al. Cobalt single atom incorporated in ruthenium oxide sphere: A robust bifunctional electrocatalyst for HER and OER. *Angew. Chem.* **2022**, *134*, e202114951.

[46] Wang, Y.; Li, X. P.; Zhang, M. M.; Zhang, J. F.; Chen, Z. L.; Zheng, X. R.; Tian, Z. L.; Zhao, N. Q.; Han, X. P.; Zaghib, K. et al. Highly active and durable single-atom tungsten-doped $NiS_{0.5}Se_{0.5}$ Nanosheet @ $NiS_{0.5}Se_{0.5}$ nanorod heterostructures for water splitting. *Adv. Mater.* **2022**, *34*, 2107053.

[47] Wang, X. Z.; Jiang, J.; Zhang, J. Y.; Zeng, Q. Y.; Liu, A. K.; Ai, L. H. Regulating d-p band center with selenium vacancy in iron diselenide nanoarrays towards sulfion-assisted seawater electrolysis for chlorine-free hydrogen production. *J. Colloid Interface Sci.* **2025**, *684*, 367–376.

[48] Tian, B.; Sun, L. G.; Zeng, Z. Y.; Ho, D. A full Volmer-Heyrovsky reaction catalyst based on sulfur vacancy structure optimization. *J. Mater. Chem. A* **2024**, *12*, 22082–22091.

[49] Zhang, T. Y.; Jin, J.; Chen, J. M.; Fang, Y. Y.; Han, X.; Chen, J. Y.; Li, Y. P.; Wang, Y.; Liu, J. F.; Wang, L. Pinpointing the axial ligand effect on platinum single-atom-catalyst towards efficient alkaline hydrogen evolution reaction. *Nat. Commun.* **2022**, *13*, 6875.

[50] Wang, F.; Gao, Y.; Jiang, Z. Q.; Tian, F.; Pang, Z. Y.; Yu, X.; Li, G. S.; Hsu, H. Y.; Hu, S.; Ji, L. et al. Bridging-induced densified MXene films with ultralow single-atom Pt loading for highly efficient hydrogen evolution. *Nano Res.* **2025**, *18*, 94907671.

[51] Wang, S. J.; Xiong, X. L.; Zou, X. L.; Ding, K.; Pang, Z. Y.; Xu, Q.; Zhou, Z. F.; Lu, X. G. Unraveling the dissolution mechanism of platinum and silver electrodes during composite electrodeposition in a deep eutectic solvent. *J. Mater. Chem. A* **2020**, *8*, 4354–4361.

[52] Su, L. X.; Wu, H.; Zhou, S. N.; Qian, R. J.; Cui, C. X.; Zhang, S. K.; Wu, L. Q.; Li, W. T.; Pang, H. Narrowing the kinetic gap between alkaline and acidic hydrogen oxidation reactions through intermediate behaviors regulated on d-p hybridized Pd-based catalysts. *Adv. Sci.* **2025**, *12*, e13616.

[53] He, D.; Wang, T. Y.; Lu, J. H.; Liu, Y.; Gu, W.; Liu, X.; Fu, C. C.; Qin, Y. T.; Li, J. B.; Liu, X. Y. et al. Protein-guided biomimetic calcification constructing 3D nitrogen-rich core–shell structures realizing high-performance lithium-sulfur batteries. *Adv. Mater.* **2025**, *37*, 2416268.

[54] Shi, Y. X.; Song, G. J.; Yang, B.; Tang, Y. J.; Liu, Z.; Zhang, Z.; Shakouri, M.; Cheng, J. B.; Pang, H. Prussian blue analogues “dressed” in MXene nanosheets tightly for high performance lithium-ion batteries. *Adv. Mater.* **2025**, *37*, 2416665.

[55] Zhang, F.; Zhao, R.; Wang, Y. R.; Han, L.; Gu, J. M.; Niu, Z. M.; Yuan, Y. M.; Qu, N. R.; Meng, J. X.; Wang, D. S. Superwettable surface-dependent efficiently electrocatalytic water splitting based on their excellent liquid adsorption and gas desorption. *Chem. Eng. J.* **2023**, *452*, 139513.

[56] Zhang, W.; Xu, G. R.; Sun, T. T.; Li, J. Y.; Miao, Y.; Wu, Z. X.; Zhang, Y.; Wang, L. Electron-rich Ru atoms in loaded Ru_4Fe intermetallic compounds/C modulate the kinetics of neutral hydrogen evolution. *Adv. Funct. Mater.* **2025**, *35*, 2501508.

[57] Fu, H. Q.; Zhou, M.; Liu, P. F.; Liu, P. R.; Yin, H. J.; Sun, K. Z.; Yang, H. G.; Al-Mamun, M.; Hu, P. J.; Wang, H. F. et al. Hydrogen spillover-bridged Volmer/Tafel processes enabling ampere-level current density alkaline hydrogen evolution reaction under low overpotential. *J. Am. Chem. Soc.* **2022**, *144*, 6028–6039.